Cerium Oxide-Decorated γ-Fe$_2$O$_3$ Nanoparticles: Design, Synthesis and *in vivo* Effects on Parameters of Oxidative Stress

Maksym Moskvin[1], Irena Marková[2], Hana Malínská[2], Denisa Miklánková[2], Martina Hüttl[2], Olena Oliyarnyk[2], Ognen Pop-Georgievski[1], Alexander Zhigunov[1], Eduard Petrovský[3] and Daniel Horák[1]*

[1] Institute of Macromolecular Chemistry, Czech Academy of Sciences, Prague, Czechia, [2] Institute for Clinical and Experimental Medicine, Prague, Czechia, [3] Institute of Geophysics, Czech Academy of Sciences, Prague, Czechia

Magnetic γ-Fe$_2$O$_3$/CeO$_x$ nanoparticles were obtained by basic coprecipitation/oxidation of iron chlorides with hydrogen peroxide, followed by precipitation of Ce(NO$_3$)$_3$ with ammonia. The appearance of CeO$_x$ on the magnetic particle surface was confirmed by X-ray photoelectron spectroscopy (XPS), powder X-ray diffraction (XRD), and elemental analysis; a magnetometer was used to measure the magnetic properties of γ-Fe$_2$O$_3$/CeO$_x$. The relatively high saturation magnetization of the particles (41.1 A·m^2/kg) enabled magnetic separation. The surface of γ-Fe$_2$O$_3$/CeO$_x$ particles was functionalized with PEG-neridronate of two different molecular weights to ensure colloidal stability and biocompatibility. The ability of the particles to affect oxidative stress in hereditary hypertriglyceridemic (HHTg) rats was tested by biological assay of the liver, kidney cortex, and brain tissues. An improvement was observed in both enzymatic [superoxide dismutase (SOD), catalase (CAT), and glutathione peroxidase (GPx)] and non-enzymatic (reduced (GSH) and oxidized (GSSG) glutathione) levels of antioxidant defense and lipid peroxidation parameters [4-hydroxynonenal (4-HNE) and malondialdehyde (MDA)]. The results corresponded with chemical determination of antioxidant activity based on 2,2-diphenyl-1-picrylhydrazyl (DPPH) assay, proving that in the animal model γ-Fe$_2$O$_3$/CeO$_x$@PEG$_{2,000}$ nanoparticles effectively scavenged radicals due to the presence of cerium oxide, in turn decreasing oxidative stress. These particles may therefore have the potential to reduce disorders associated with oxidative stress and inflammation.

Keywords: maghemite, cerium oxide, nanoparticles, oxidative stress, antioxidant

INTRODUCTION

On a cellular level, many types of inflammation are associated with the excessive formation of reactive oxygen species (ROS) such as superoxide/hydroxyl radicals and hydrogen peroxide (H$_2$O$_2$) (Schieber and Chandel, 2014). Their ability to be scavenged is important in combating serious oxidative stress-related diseases, such as atherosclerosis, liver steatosis, diabetes mellitus, cancer, Alzheimer's disease, and aging. All these disorders are associated with severe damage to lipids, proteins, and nucleic acids (Poprac et al., 2017; Rehman and Akash, 2017). Due to ability of

cerium oxide (CeO_x) nanoparticles to mimic antioxidant enzymes such as superoxide dismutase (SOD) (Korsvik et al., 2007; Celardo et al., 2011), catalase (CAT) (Pirmohamed et al., 2010), and peroxidase (Jiao et al., 2012), they have recently received considerable attention as a potentially useful antioxidant agent in mitigating these diseases. These nanoparticles are adept at scavenging almost all types of reactive species, including hydroxyl and nitroxyl radicals. The impressive radical scavenging activity of CeO_x, which can take the form of CeO_2 or Ce_2O_3, is attributed to mutations in the oxidation state between Ce^{4+} and Ce^{3+} ions (Asati et al., 2009; Xu and Qu, 2014). In order to enhance scavenging activity, the surface area of CeO_x must be increased, achieved by decreasing their overall size to a nanometer scale.

In addition to their usefulness in biomedicine, drug delivery, and analysis, CeO_x nanoparticles are also utilized in numerous engineering applications, such as solid-oxide fuel and solar cells (Stambouli and Traversa, 2002; Corma et al., 2004), corrosion protection (Ivanov et al., 2009), and catalysis (Walkey et al., 2015). The many approaches to preparing CeO_x nanoparticles largely depend on variations in morphology, size, and the tendency to aggregate. These include ball milling, thermal decomposition, precipitation, spray pyrolysis, hydro-/solvothermal or sol-gel methods, surfactant-assisted techniques, and green synthesis using natural stabilizers (Xu and Qu, 2014). Precursors of CeO_x synthesis include ammonium cerium nitrate, cerium sulfate, nitrate, and chloride. However, a key role in the fabrication of CeO_x nanoparticles is played by surface engineering, which ensures colloidal stability in physiological media, biocompatibility, and/or functionalization with reactive groups employed for further conjugation of biomolecules, targeting peptides, and/or drugs. Among the conventionally used coatings are dextran (Karakoti et al., 2007; Weaver and Stabler, 2015), polyethylenimin (Lee et al., 2013), poly(ethylene glycol) (Karakoti et al., 2009), poly(acrylic acid) (Wu et al., 2018), cyclodextrin (Xu et al., 2013), and glucose (Li et al., 2013).

Another class of inorganic particles attracting growing attention in biomedicine is the iron oxides (magnetite Fe_3O_4 and maghemite γ-Fe_2O_3). These materials are superparamagnetic, magnetizing in the presence of an external magnetic field; however, they exhibit no residual magnetization in the absence of a magnetic field (Li et al., 2017). These properties enable the targeting tissues required by drug delivery systems and/or monitoring of iron oxide-labeled cells using non-invasive *in vivo* magnetic resonance imaging (MRI). Moreover, magnetic nanoparticles can control the movement and transportation of biomolecules and/or generate heat in an external magnetic field to kill tumor cells (Jordan et al., 1993). A major advantage of Fe_3O_4 and γ-Fe_2O_3 is their biocompatibility, with ferumoxytol (Feraheme) approved by the US Food and Drug Administration in 2009 for the treatment of patients with chronic kidney disease suffering from iron deficiency (Toth et al., 2017).

The aim of this report was to merge both the magnetic and antioxidant properties of the maghemite core and cerium oxide shell into a new delivery system that would be colloidally stable and magnetically manipulable. Antioxidant properties were verified based on chemical and biological *in vivo* tests of

using a rat model of metabolic syndrome and prediabetes— the hereditary hypertriglyceridaemic rat (Malinska et al., 2019). Effect of cerium oxide-decorated γ-Fe_2O_3 nanoparticles on oxidative stress and antioxidant defense parameters has been evaluated.

EXPERIMENTAL

Materials

$FeCl_2 \cdot 4H_2O$, $FeCl_3 \cdot 6H_2O$, $Ce(NO_3)_3 \cdot 6H_2O$, trisodium citrate dihydrate, and 2,2-diphenyl-1-picrylhydrazyl (DPPH) were purchased from Sigma-Aldrich (St. Louis, MO, USA). NH_4OH (25 wt.%), HCl (35 wt.%), H_2O_2 (30 wt.%), ethanol (96 %), propan-2-ol, and all other chemicals were purchased from LachNer (Neratovice, Czechia). Poly(ethylene glycol)-neridronate (PEG-Ner) was synthesized using PEG at a molecular weight of 2,000 or 5,000 Da as described previously (Kostiv et al., 2017).

Preparation of Cerium Oxide-Decorated Maghemite Nanoparticles (γ-Fe_2O_3/CeO_x)

γ-Fe_2O_3 cores were obtained by modifying a previously published procedure (Moskvin and Horák, 2016). Briefly, an aqueous $FeCl_3$ and $FeCl_2$ solution (500 ml; $FeCl_3$/$FeCl_2$ = 2/1 mol/mol) was precipitated with NH_4OH (20 ml; pH 11) at 70°C by stirring (700 rpm); the resulting magnetite (Fe_3O_4) was oxidized by the addition of H_2O_2 (5 ml) and 35 % HCl (~12 ml) at 90°C. The final γ-Fe_2O_3 particles were washed with water five times using a magnetic separation and sonication (Hielscher UP-400St; Teltow, Germany; 20 W and 70 % amplitude) for 10 min and stabilized with trisodium citrate (60 mg per 300 mg of γ-Fe_2O_3). The γ-Fe_2O_3 surface was then modified by dispersion precipitation of cerium(III) nitrate (300 mg; γ-Fe_2O_3/$Ce(NO_3)_3$ = 1/1 w/w) with NH_4OH (1 ml; pH 11) in a mixture of water/propan-2-ol = 1/1 v/v (25 ml) at 60°C for 3 h. Subsequently, the colloid was thoroughly washed with water 10 times (20 ml each) under sonication and magnetic separation and stabilized by the addition of aqueous trisodium citrate as described above; the final concentration was 4 mg of γ-Fe_2O_3/CeO_x per ml (pH ~8).

Pure CeO_x particles used as a reference material in DPPH assay were prepared as described above, but in the absence of γ-Fe_2O_3.

PEGylation of Cerium Oxide-Decorated Maghemite Nanoparticles (γ-Fe_2O_3/CeO_x@PEG)

Aqueous γ-Fe_2O_3/CeO_x (100 mg) dispersion (10 ml) was added to a solution of poly(ethylene glycol)-neridronate (40 mg) in water (15 ml). The reaction proceeded at room temperature (RT) for 1 h with sonication for 5 min. The resulting γ-Fe_2O_3/CeO_x@$PEG_{2,000}$ and γ-Fe_2O_3/CeO_x@$PEG_{5,000}$ nanoparticles were washed with water (100 ml).

Particle Characterization

γ-Fe_2O_3 nanoparticles were visualized using the Tecnai G2 Spirit transmission electron microscope (TEM; FEI; Brno, Czechia).

Number-average diameter ($D_n = \Sigma D_i/N$, where D_i is the diameter of the i-th particle and N is the total number of particles), weight-average diameter ($D_w = \Sigma D_i^4/\Sigma D_i^3$) and dispersity ($Đ = D_w/D_n$) were calculated from at least 300 individual particles on the micrographs using Atlas software (Tescan Digital Microscopy Imaging; Brno, Czechia). Surface ζ-potential, hydrodynamic diameter D_h, and polydispersity PI were measured by dynamic light scattering (DLS) using a ZEN3600 Nano-ZS ZetaSizer (Malvern Instruments; Malvern, Worcestershire, UK).

The X-ray diffraction (XRD) patterns of dry γ-Fe$_2$O$_3$, γ-Fe$_2$O$_3$/CeO$_x$, and γ-Fe$_2$O$_3$/CeO$_x$@PEG$_{2,000}$ particles were measured in reflection mode using the Explorer high-resolution diffractometer (GNR Analytical Instruments; Agrate Conturbia, Italy) equipped with the Mythen 1K one-dimensional silicon strip detector (Dectris; Baden, Switzerland). Radiation of MoKα ($\lambda = 0.7107$ Å) monochromatized with Zr foil (β-filter) was used for diffraction in the range of $2\theta = 2$–$40°$ with step $0.1°$ and exposure time 10 s. FTIR spectra were recorded in KBr pellet on a Bruker IFS 55 spectrometer (Billerica, MA, USA) with a DTGS detector under resolution of 4 cm^{-1} and 32 scans. Cerium, iron, carbon, hydrogen and nitrogen content was determined using the Perkin-Elmer 3110 atomic absorption spectrometer after mineralizing particles with HCl (1:1) at 80°C and the Perkin-Elmer 2400 CHN elemental analyzer. Magnetic properties of the particles were measured using the EV9 vibrating sample magnetometer (DSM Magnetics ADE; Lowell, MA, USA) at RT; magnetization was corrected for paramagnetic contribution in fields >400 kA/m.

X-ray Photoelectron Spectroscopy (XPS)

XPS was performed using a K-Alpha$^+$ XPS spectrometer (Thermo Fisher Scientific; Loughborough, UK) operating at a base pressure of 1.0×10^{-7} Pa. Data were acquired and processed using Thermo Scientific Avantage software. γ-Fe$_2$O$_3$, γ-Fe$_2$O$_3$/CeO$_x$, and γ-Fe$_2$O$_3$/CeO$_x$@PEG$_{2,000}$ nanoparticles were uniformly deposited on clean silicon substrates and analyzed using Al Kα X-ray microfocused monochromated radiation (400 μm spot size) with a pass energy of 200 and 50 eV for survey and high-energy resolution core-level spectra, respectively. The X-ray angle of incidence was 30°, with the emission angle normal to the surface. The K-Alpha dual-charge compensation system was employed during analysis, using electrons and low-energy argon ions to prevent any localized charge build-up. The acquisition times were kept <1 min to avoid the reduction of cerium oxide after the exposure to XPS radiation under high vacuum (Zhang et al., 2004). The high-resolution spectra were fitted using Voigt profiles and referenced to the C 1s peak attributed to C-C and C-H at 285.0 eV binding energy, which was controlled using the standard photoelectron peak positions for poly(ethylene terephthalate), Cu, Ag, and Au. Atomic concentrations of phosphorous, carbon, nitrogen, oxygen, iron, and cerium were determined from the P 2p, C 1s, N 1s, O 1s, Fe 2p, and Ce 3d photoelectron peak areas after Shirley inelastic background subtraction. The amount of cerium in oxidation states Ce^{3+} and Ce^{4+} was approximated by comparing the measured spectra with those of Ce$_2$O$_3$ and CeO$_2$ taken from Avantage database.

DPPH Radical Scavenging Assay

The antioxidant activity of the particles was measured colorimetrically by 2,2-diphenyl-l-picrylhydrazyl (DPPH) assay. Briefly, 0.1 mM ethanolic DPPH solution (0.6 ml) was added in a 2 ml Eppendorf tube to a mixture of ethanol (1.2 ml) and aqueous particle dispersion (0.2 ml; 4.4 mg of γ-Fe$_2$O$_3$/ml) with shaking for 1 min using a Vortex shaker (1,000 rpm), leaving the reaction to continue in darkness for 30 min. The above mixture was used as a control or blank solution in the absence of the particles or DPPH, respectively. Absorbance of the solution was measured by the Specord 250 Plus UV-Vis spectrophotometer (Analytik Jena, Germany) against ethanol at 517 nm. Antioxidant activity (AA) was calculated using Equation (1):

$$AA = \frac{A_c - A_p + A_b}{A_c} \cdot 100 \qquad (1)$$

where A_c, A_p, and A_b is the absorption of control, particle dispersion, and blank, respectively.

Administration of γ-Fe$_2$O$_3$/CeO$_x$ Nanoparticles Using an Experimental Animal Model

To investigate the *in vivo* effect of cerium oxide nanoparticles, a non-obese rat model of metabolic syndrome and prediabetes was used. The hereditary hypertriglyceridemic (HHTg) strain of rat exhibits dyslipidemia, tissue resistances to insulin action, fatty liver, mild hypertension, and low-grade chronic inflammation in the absence of obesity. Animals were fed a standard diet and given free access to food and water. Five-month-old male rats were randomly divided into five experimental groups of eight animals; untreated rats, treated with γ-Fe$_2$O$_3$ (control), γ-Fe$_2$O$_3$/CeO$_x$, γ-Fe$_2$O$_3$/CeO$_x$@PEG$_{2,000}$, and γ-Fe$_2$O$_3$/CeO$_x$@PEG$_{5,000}$ nanoparticles. Nanoparticle dispersions (4 mg/ml) were administrated i.v. to the *vena caudalis* at a dose of 0.5 ml, untreated rats were given i.v. 0.5 ml saline instead of nanoparticle dispersion. Three days after nanoparticle application, the animals were sacrificed in a postprandial state. The collected tissue samples (liver, kidney cortex and brain) were immediately frozen in liquid nitrogen and stored at −80°C before analysis.

All experiments were performed in agreement with the Animal Protection Law of the Czech Republic (311/1997) in compliance with European Community Council recommendations (86-609/ECC) for the use of laboratory animals and approved by the Ethics Committee of the Institute for Clinical and Experimental Medicine, Prague.

Basal Metabolic Analysis

Serum levels of triglycerides, glucose, and total cholesterol were measured using commercially available kits (Erba Lachema; Brno, Czechia). Alanine aminotransferase (ALT) and aspartate
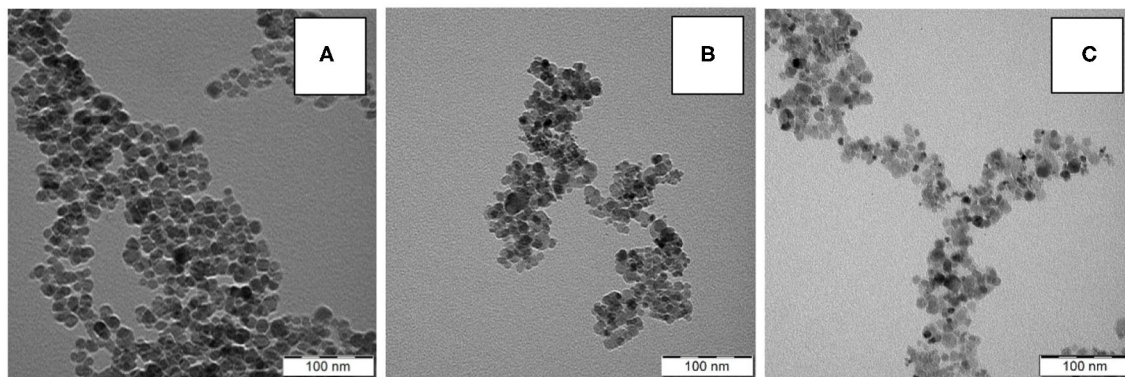
FIGURE 1 | TEM micrographs of **(A)** γ-Fe_2O_3, **(B)** γ-Fe_2O_3/CeO_x, and **(C)** γ-Fe_2O_3/CeO_x@$PEG_{2,000}$ nanoparticles.

TABLE 1 | Characterization of nanoparticles.

Particles	D_n (nm)	Đ	D_h (nm)	PI	ζ-potential (mV)	AA (%)
γ-Fe_2O_3	15	1.28	68	0.21	−43	13
γ-Fe_2O_3/CeO_x	16 (6)[a]	1.33	85	0.27	−45	78
γ-Fe_2O_3/CeO_x@$PEG_{2,000}$	16 (6)[a]	1.39	63	0.20	−29	89
γ-Fe_2O_3/CeO_x@$PEG_{5,000}$	17 (6)[a]	1.37	71	0.22	−15	85

[a]CeO_x nanoparticles; D_n, number-average particle diameter (TEM); Đ, dispersity (TEM); D_h, hydrodynamic diameter (DLS); PI, polydispersity (DLS); AA, antioxidant activity.

aminotransferase (AST) enzyme activity was determined spectrophotometrically using routine clinical biochemistry methods and Roche Diagnostics kits (Mannheim, Germany).

Oxidative Stress Parameters

Levels of reduced (GSH) and oxidized (GSSG) forms of glutathione were determined by high-performance liquid chromatography (HPLC) with fluorescent detection using a HPLC diagnostic kit (Chromsystems; Gräfelfing, Germany).

The antioxidant enzyme activity of superoxide dismutase (SOD), catalase (CAT), and glutathione peroxidase (GPx) was measured using commercially available kits (Sigma-Aldrich and Cayman Chemicals; Ann Arbor, MI, USA). Malondialdehyde (MDA), a parameter of lipid peroxidation, was determined by HPLC with fluorescence detection; 4-hydroxynonenal (4-HNE), a sensitive product of lipid peroxidation, was detected by rat ELISA assay (MyBiosource; San Diego, CA, USA).

Statistical Analysis

All data were expressed as mean ± SEM. Statistical analysis was performed by one-way ANOVA with Fisher's *post-hoc* test using Statistica 12 software. Group comparisons were made against the control group of γ-Fe_2O_3-administered animals. Statistical significance was defined as $p < 0.05$.

RESULTS

γ-Fe_2O_3 Nanoparticles

Starting iron oxide particles were prepared using a one-pot procedure consisting of two steps: (*i*) aqueous precipitation of Fe(II) and Fe(III) chlorides with ammonia, followed by (*ii*) oxidation with H_2O_2 and electrostatic stabilization achieved by the addition of trisodium citrate. The morphology of particles was almost spherical, with a mean diameter $D_n = 15$ nm and a dispersity Đ $= 1.28$ according to TEM, indicating moderately broad particle size distribution (**Figure 1A**; **Table 1**). These results were in agreement with DLS analysis, which documented polydispersity $PI = 0.21$, hydrodynamic size $D_h = 68$ nm, and ζ-potential $= -43$ mV due to citrate stabilization. D_h proved larger than D_n because the former is a z-average diameter affected by the presence of larger particles to a much greater extent than the latter diameter of dry particles determined by TEM. Moreover, the particles had a tendency to slight aggregation in water.

To determine whether magnetite (Fe_3O_4) or maghemite (γ-Fe_2O_3) was obtained during coprecipitation, an XRD diffractogram of the synthesized iron oxide particles was compared with the reference diffraction lines of cubic γ-Fe_2O_3 according to the Crystallography Open Database (COD)[1]; COD ID 96-900-6317 (**Figure 2**; reference vertical diffraction lines were marked in black). The most intense peaks for Fe_3O_4 and γ-Fe_2O_3 coincided; the differences in peak positions were minor, but clearly visible, suggesting that the particles contained

---

[1]http://www.crystallography.net/cod/9012692.html

γ-Fe$_2$O$_3$. The less intense γ-Fe$_2$O$_3$ peak, at $2\theta = 22.49°$, was observed as a small bump in the diffractogram. The particle sizes L were estimated using the Scherrer (Equation 2):

$$L = \frac{K\lambda}{\beta \cdot \cos\Theta} \qquad (2)$$

where K is the shape factor (usually 0.9) and β is the full width at half maximum (FWHM) of reflection. For this purpose, the most intense peak at $2\theta = 16.24°$ was chosen, possessing FWHM $= 0.4734°$. Assuming that the particle is fully crystalline, average size of 17.4 nm was obtained, which agrees well with TEM results.

Cerium Oxide-Decorated γ-Fe$_2$O$_3$ Nanoparticles (γ-Fe$_2$O$_3$/CeO$_x$)

A TEM micrograph of γ-Fe$_2$O$_3$/CeO$_x$ particles could not distinguish CeO$_x$ from γ-Fe$_2$O$_3$ due to their similar electron densities (**Figure 1B**); however, rather small CeO$_x$ nanoparticles ($\sim$6 nm) were clearly visible in the micrograph in addition to the pure γ-Fe$_2$O$_3$ particles (**Figure 1A**). Neither the dispersity ($Đ = 1.33$) nor morphology of the γ-Fe$_2$O$_3$/CeO$_x$ particles (**Figure 1B**) substantially differed from those of starting γ-Fe$_2$O$_3$. This was in agreement with results obtained on magnetic cerium oxide nanoconjugates prepared by glutaraldehyde-crosslinked polyethyleneimine-coated mixture of magnetic and cerium oxide nanoparticles (Turin-Moleavin et al., 2019). Compared to the γ-Fe$_2$O$_3$ particles, the hydrodynamic size of γ-Fe$_2$O$_3$/CeO$_x$ nanoparticles in water increased ($D_h = 85$ nm), probably due to the presence of CeO$_x$ and the citrate layer; ζ-potential did not substantially change from that of γ-Fe$_2$O$_3$.

From the XRD spectrum of γ-Fe$_2$O$_3$/CeO$_x$ nanoparticles, it was evident that CeO$_2$ was present in the composite in its crystalline form (**Figure 2**). The conclusion was made by comparing the diffractogram with COD ID 96-434-3162. Therefore, the diffraction curve, corresponding to the γ-Fe$_2$O$_3$/CeO$_x$ composite (**Figure 2**, red line), showed the superposition of neat crystalline phases of γ-Fe$_2$O$_3$ and CeO$_2$.

FTIR spectra of the γ-Fe$_2$O$_3$ and γ-Fe$_2$O$_3$/CeO$_x$ particles were recorded to probe their surface structure (**Figure 3**); the spectra did not substantially differ, with the exception of high intensities of γ-Fe$_2$O$_3$ bands in the region of 400–800 cm^{-1}, corresponding to the vibrations of atoms in the crystalline lattice of iron oxide. A broad band of OH- stretching vibrations was situated at $\sim$3,400 cm^{-1} and ascribed to hydroxyl groups on the particle surface and partially to water adsorbed by hygroscopic KBr used as a binder for the sample preparation.

The covalent structure of the nanoparticles was further investigated after each modification step by XPS (**Figure 4**; **Table 2**). The pure γ-Fe$_2$O$_3$ nanoparticles exhibited a characteristic Fe 2p spectrum previously reported for maghemite (Zasonska et al., 2016; Shatan et al., 2019). Successful deposition of cerium oxide on γ-Fe$_2$O$_3$ was verified in the high-resolution Ce 3d spectra of γ-Fe$_2$O$_3$/CeO$_x$ nanoparticles based on the appearance of characteristic Ce 3d$_{5/2}$-Ce 3d$_{3/2}$ spin-orbital multiplet splitting. Ce content reached $\sim$26 wt.%, while iron

content in the γ-Fe$_2$O$_3$/CeO$_x$ particles dropped to 38.7 ± 1.7 wt.% from 64.5 ± 2.2 wt.% in γ-Fe$_2$O$_3$. The Ce^{4+}/Ce^{3+} ratio was determined to be 7.8 (**Table 2**), showing that cerium was predominantly in the form of CeO$_2$ ($\sim$23.1 wt.%). Small peaks were found in the C 1s spectra of pure γ-Fe$_2$O$_3$ and γ-Fe$_2$O$_3$/CeO$_x$ nanoparticles, originating from organic molecules adsorbed on the nanoparticle surface during its exposure to air.

Magnetic measurements of γ-Fe$_2$O$_3$ and γ-Fe$_2$O$_3$/CeO$_x$ nanoparticles revealed saturation magnetization values of $M_s = 53.3$ and 41.1 A·m^2/kg, respectively (**Figure 5**). This means that $\sim$23 wt.% of CeO$_x$ was present in the γ-Fe$_2$O$_3$/CeO$_x$ particles, as calculated from the dependence of M_s on γ-Fe$_2$O$_3$ content. Remanent magnetization and coercivity of γ-Fe$_2$O$_3$ and γ-Fe$_2$O$_3$/CeO$_x$ were very low ($M_{rs} = 0.4$ and
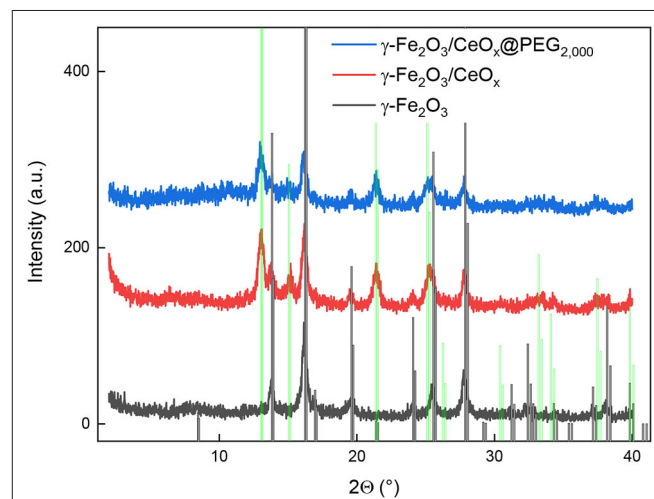
FIGURE 2 | Diffraction pattern of γ-Fe$_2$O$_3$ (black), γ-Fe$_2$O$_3$/CeO$_x$ (red), and γ-Fe$_2$O$_3$/CeO$_x$@PEG$_{2,000}$ nanoparticles (blue) compared to that of γ-Fe$_2$O$_3$ and CeO$_2$ from the Crystallography Open Database (vertical black and green lines, respectively).
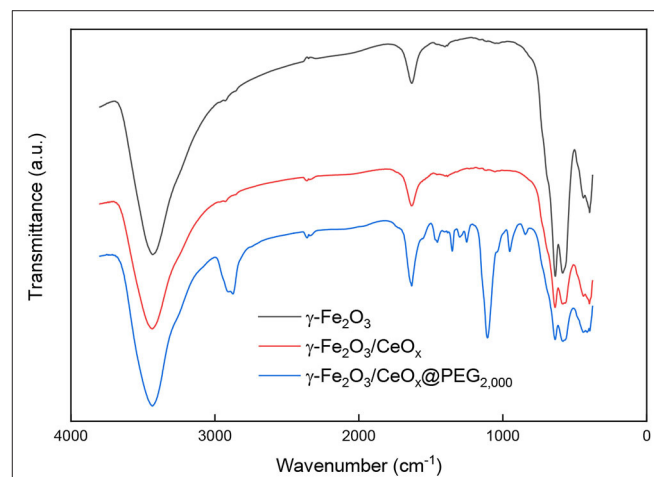

FIGURE 3 | FTIR spectra of γ-Fe$_2$O$_3$, γ-Fe$_2$O$_3$/CeO$_x$, and γ-Fe$_2$O$_3$/CeO$_x$@PEG$_{2,000}$ nanoparticles.
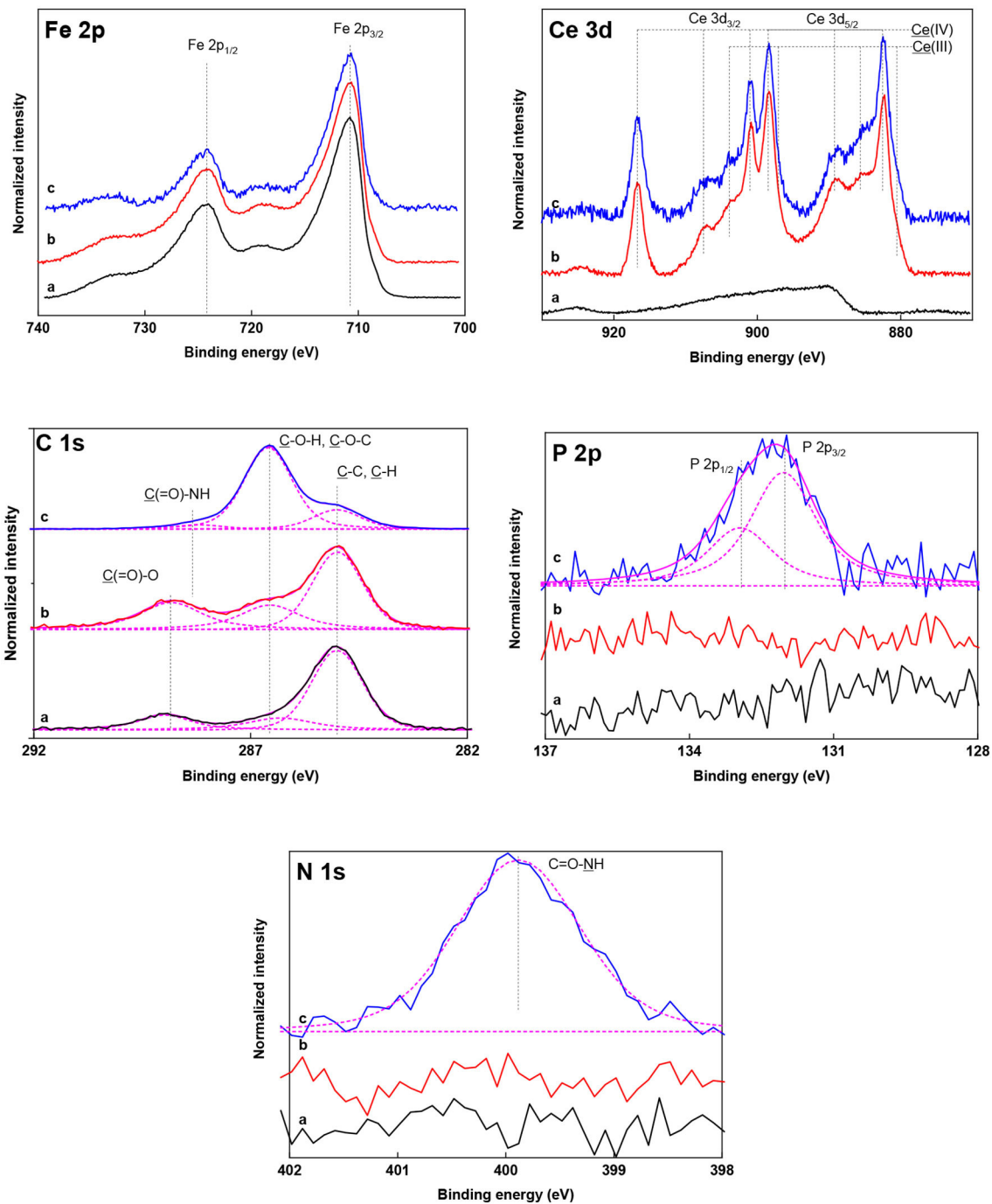
FIGURE 4 | High-resolution Fe 2p, Ce 3d, C 1s, P 2p, and N 1s XPS spectra of (a) γ-Fe$_2$O$_3$, (b) γ-Fe$_2$O$_3$/CeO$_x$, and (c) γ-Fe$_2$O$_3$/CeO$_x$@PEG$_{2,000}$ nanoparticles. Spectra and their resulting fitted envelopes are presented with full and magenta lines, respectively. Individual contributions of the fitted curve are presented with dashed lines.

0.2 A·m^2/kg and H_c = 2.8 and 1.1 Oe, respectively), as determined using interpolation between the neighboring data points on the hysteresis loop. This shows the absence of a domain structure due to the collective behavior and high concentration of superparamagnetic particles. As a result, the particles remained dispersible in water in the absence of an external magnetic field

and easily magnetized and manipulated in its presence, thus enabling magnetic separation of the γ-Fe$_2$O$_3$/CeO$_x$ particles.

γ-Fe$_2$O$_3$/CeO$_x$@PEG Nanoparticles

To provide efficient steric stabilization even in buffered media at a high ionic strength and to enhance biocompatibility

TABLE 2 | Surface composition of γ-Fe$_2$O$_3$, γ-Fe$_2$O$_3$/CeO$_x$, and γ-Fe$_2$O$_3$/CeO$_x$@PEG$_{2,000}$ nanoparticles determined by XPS analysis.

Electronic state of element	γ-Fe$_2$O$_3$ (wt.%)	γ-Fe$_2$O$_3$/CeO$_x$ (wt.%)	γ-Fe$_2$O$_3$/CeO$_x$@PEG$_{2,000}$ (wt.%)
P 2p	–[a]	–	1.8 ± 0.1
C 1s	7.5 ± 1.9	8.8 ± 1.2	34.0 ± 0.5
			26.1 ± 0.1[b]
N 1s	–	–	0.9 ± 0.1
O 1s	28.0 ± 0.4	26.2 ± 0.8	36.2 ± 0.2
Fe 2p	64.5 ± 2.2	38.7 ± 1.4	13.9 ± 0.2
Ce 3d	–	26.3 ± 0.7	13.2 ± 0.4
Ce^{4+}/Ce^{3+}	–	7.8 ± 0.1	7.7 ± 0.2

[a]Below the detection limit of XPS measurement; [b]content of PEG according to C-O-C bond.
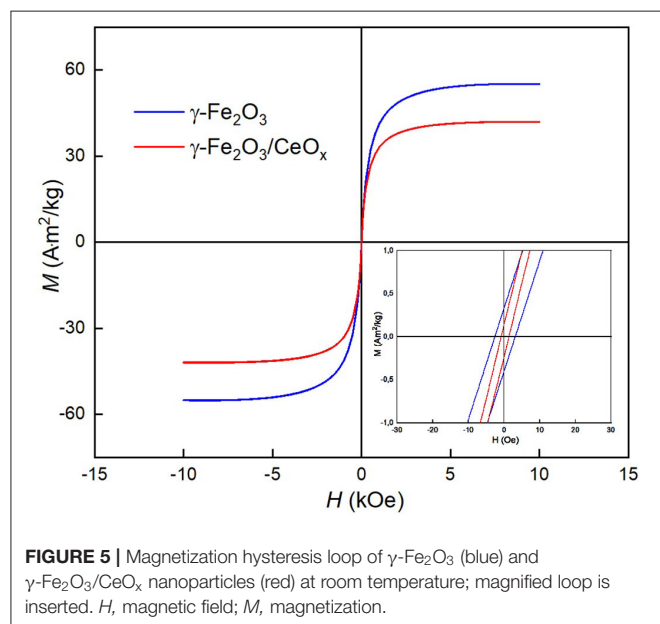
FIGURE 5 | Magnetization hysteresis loop of γ-Fe$_2$O$_3$ (blue) and γ-Fe$_2$O$_3$/CeO$_x$ nanoparticles (red) at room temperature; magnified loop is inserted. H, magnetic field; M, magnetization.

of the γ-Fe$_2$O$_3$/CeO$_x$ nanoparticles, their surfaces were modified with PEG-neridronate (PEG-Ner) at two different molecular weights: M_w = 2,000 and 5,000 Da (**Figure 6**). PEG-Ner was obtained from sodium neridronate and O-[(N-succinimidyl)succinylaminoethyl]-O'-methylpoly(ethylene glycol) as previously described (Kostiv et al., 2017). As PEG <5 kDa is typically used for PEGylation of particles in *in vivo* studies (Zalipsky, 1995), γ-Fe$_2$O$_3$/CeO$_x$@PEG$_{2,000}$ particles were investigated by TEM, XPS, FTIR, and elemental analysis. According to TEM, γ-Fe$_2$O$_3$/CeO$_x$@PEG$_{2,000}$ nanoparticles resembled to γ-Fe$_2$O$_3$/CeO$_x$, with PEG coating invisible due to its low electron density (**Figure 1C**). The γ-Fe$_2$O$_3$/CeO$_x$@PEG$_{2,000}$ particles had a number-average diameter D_n = 15 and 6 nm for maghemite and cerium oxide particles, respectively; dispersity Đ = 1.39 was higher than that of pure γ-Fe$_2$O$_3$ nanoparticles due to the presence of tiny CeO$_x$ particles; the hydrodynamic diameter of the γ-Fe$_2$O$_3$/CeO$_x$@PEG$_{2,000}$ and γ-Fe$_2$O$_3$/CeO$_x$@PEG$_{5,000}$

nanoparticles reached D_h = 63 and 71 nm, respectively, with PI = 0.2 (**Table 1**). The PEG-modified particles were smaller in size, as they have a reduced tendency to aggregate due to improved steric stabilization. Moreover, the effect of the counter-ion layer on citrate-stabilized γ-Fe$_2$O$_3$/CeO$_x$ particles may have caused them to increase in size. Absolute value of ζ-potential of PEGylated γ-Fe$_2$O$_3$/CeO$_x$ particles decreased due to the presence of electroneutral PEG shell; nevertheless, it was still negative (**Table 1**).

X-ray diffraction spectrum of γ-Fe$_2$O$_3$/CeO$_x$@PEG$_{2,000}$ nanoparticles was presented in **Figure 2** as a blue curve. Peak positions and relative intensities of γ-Fe$_2$O$_3$ and CeO$_2$ phases were the same as for the γ-Fe$_2$O$_3$/CeO$_x$, confirming no changes in crystalline structure of the two components. Despite the fact that the content of PEG$_{2,000}$ was relatively high (>26 wt.% according to XPS), no crystalline peak corresponding to PEG was observed. Moreover, there was a wide peak with a mean value of 2θ = 12.3°, which could be ascribed to the mean distance between PEG chains.

FTIR spectrum of γ-Fe$_2$O$_3$/CeO$_x$@PEG$_{2,000}$ nanoparticles had strong valence vibration band of amide N-H bonds at 1,550 cm^{-1}, corresponding to PEG-neridronate linker (**Figure 3**). Bands at 2,870, 1,467, and 1,342 cm^{-1} were ascribed to PEG aliphatic chain vibrations of CH$_3$ and scissor and wagging vibrations of CH$_2$, respectively. Vibrations of C-O-C groups of PEG were observed at 1,240, 1,097, and 960 cm^{-1}. Band at 1,643 and 1,278 cm^{-1} was attributed to vibrations of amide carbonyls and P=O bonds originating from phosphonic acid residues of neridronate. This confirmed successful anchoring of PEG-Ner to the particle surface.

XPS spectroscopy confirmed the successful chelation of PEG-Ner to the cerium oxide shell. The strong binding of PEG$_{2,000}$-Ner to γ-Fe$_2$O$_3$/CeO$_x$ nanoparticles was clearly evident from high-resolution P 2p, C 1s, and N 1s spectra of γ-Fe$_2$O$_3$/CeO$_x$@PEG$_{2,000}$ particles (**Figure 4**). The presence of neridronate was detected based on its characteristic P 2p and N 1s signals from the bisphosphonate and amide groups at 132.1 and 399.8 eV, respectively. The experimentally found bisphosphonate/amide ratio (0.92 mol/mol) corresponded with the theoretical ratio in PEG-Ner that equaled one. PEG binding to the cerium oxide shell induced a significant increase of
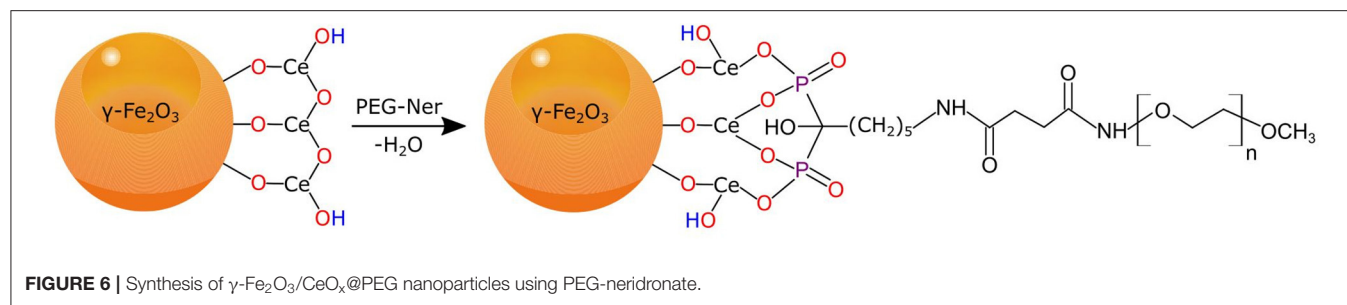
FIGURE 6 | Synthesis of γ-Fe$_2$O$_3$/CeO$_x$@PEG nanoparticles using PEG-neridronate.

TABLE 3 | Elemental composition of γ-Fe$_2$O$_3$/CeO$_x$ and γ-Fe$_2$O$_3$/CeO$_x$@PEG$_{2,000}$ nanoparticles.

Element particles	Fe (wt.%)[a]		Ce (wt.%)[a]		C (wt.%)		H (wt.%)		N (wt.%)	
	Th.	Exp.	Th.	Exp.	Th.	Exp.	Th.	Exp.	Th.	Exp.
Fe$_2$O$_3$/CeO$_x$	50	54.2	23.3	20.1	–	–	–	–	–	–
γ-Fe$_2$O$_3$/CeO$_x$@PEG$_{2,000}$	35.6	39.5	16.6	14.3	14.4	12.7	2.4	3.2	0.3	0.5

[a]Based on atomic absorption spectroscopy; Th., theoretical content, Exp., experimentally found content.

TABLE 4 | Basal metabolic parameters of HHTg animals untreated and treated with γ-Fe$_2$O$_3$/CeO$_x$-based nanoparticles.

	Untreated	γ-Fe$_2$O$_3$	γ-Fe$_2$O$_3$/CeO$_x$	γ-Fe$_2$O$_3$/CeO$_x$@PEG$_{2,000}$	γ-Fe$_2$O$_3$/CeO$_x$@PEG$_{5,000}$	p
Body weight (g)	405 ± 13	386 ± 46	387 ± 25	417 ± 36	408 ± 18	n.s.
Triacylglycerols (mmol/l)	3.22 ± 0.33	3.47 ± 0.20	3.45 ± 0.46	3.84 ± 0.34	2.96 ± 0.62	n.s.
Cholesterol (mmol/l)	1.88 ± 0.10	2.04 ± 0.35	1.86 ± 0.19	1.98 ± 0.10	1.85 ± 0.12	n.s.
Non-fasting glucose (mmol/l)	8.71 ± 0.22	8.05 ± 1.60	8.13 ± 0.38	8.70 ± 0.44	7.96 ± 0.60	n.s.
ALT (μkat/l)	1.16 ± 0.12	1.07 ± 0.08	1.09 ± 0.14	1.04 ± 0.06	1.19 ± 0.50	n.s.
AST (μkat/l)	2.75 ± 0.09	2.41 ± 0.11	2.70 ± 0.48	2.25 ± 0.18	2.76 ± 0.07	n.s.

ALT, alanine aminotransferase; AST, aspartate aminotransferase; p, statistical significance; n.s., not significant.
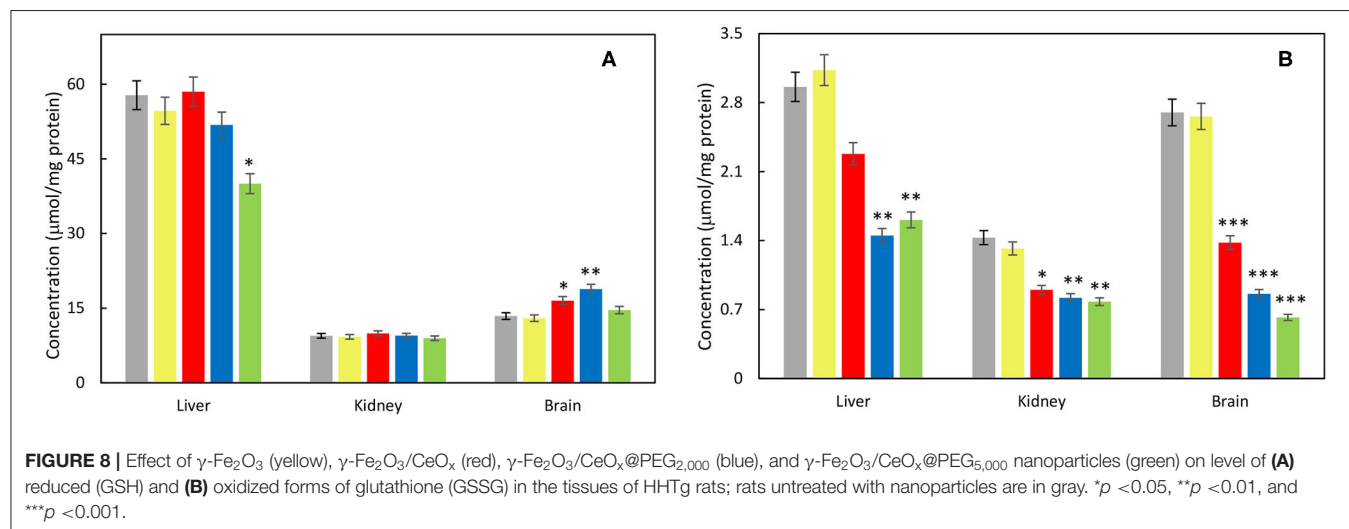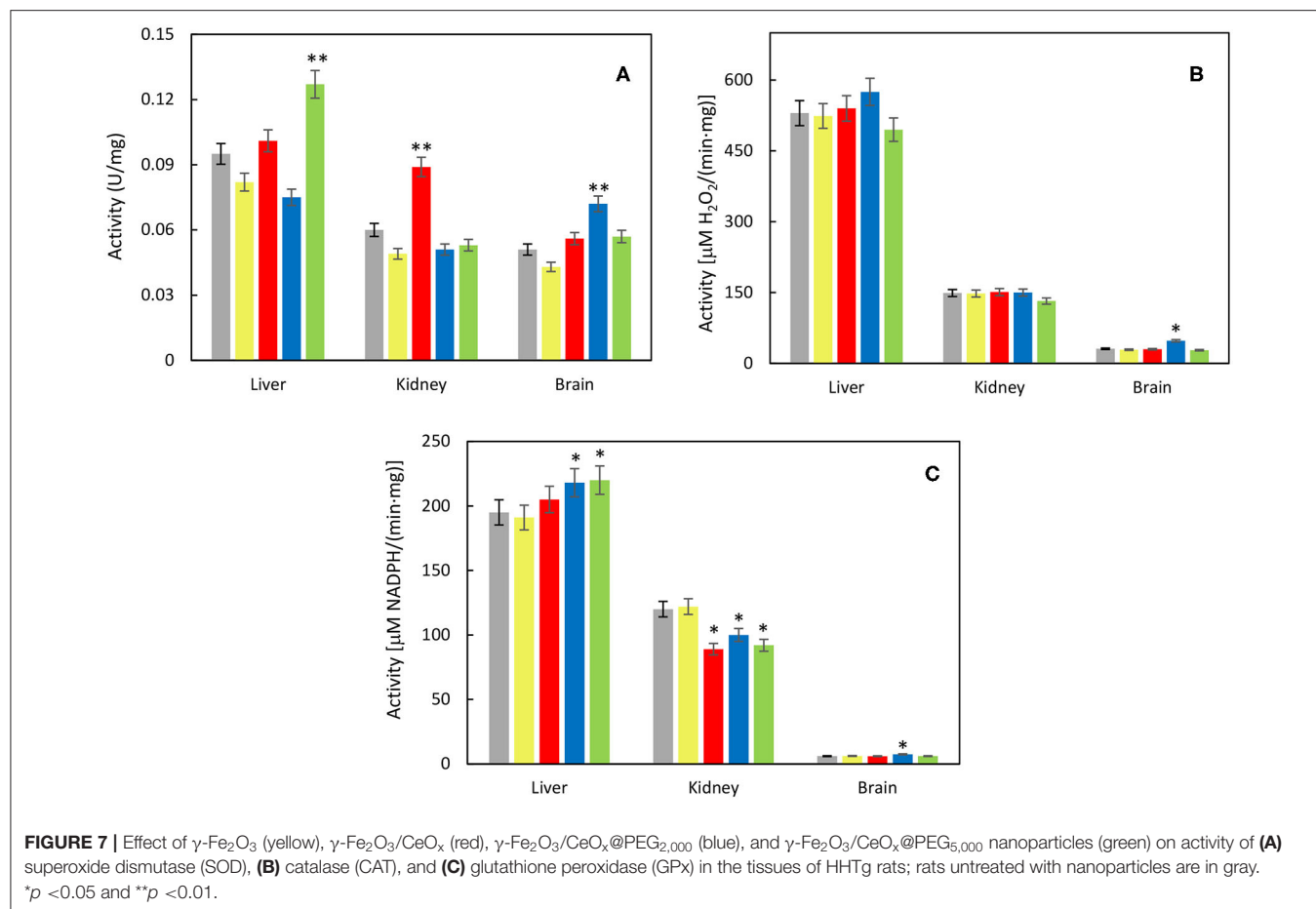
C 1s content to 34.0 ± 0.5 wt.% (**Table 2**). In addition, the C 1s spectrum of the γ-Fe$_2$O$_3$/CeO$_x$@PEG$_{2,000}$ particles was dominated by a characteristic PEG C–O–C signal at 286.6 eV (Pop-Georgievski et al., 2018); PEG reached a quantity of 26.1 ± 0.1 wt.%. Coating the γ-Fe$_2$O$_3$/CeO$_x$ with PEG induced a drop in iron and cerium content to 13.9 ± 0.2 and 13.2 ± 0.4 wt.%, respectively, further confirming the successful surface modification of the γ-Fe$_2$O$_3$/CeO$_x$ particles with PEG. Modification of the particles with PEG did not significantly reduce the Ce^{4+}/Ce^{3+} ratio amounting to 7.7 (**Table 2**). This result confirmed that the γ-Fe$_2$O$_3$/CeO$_x$ possessed high CeO$_2$ content ($\sim$11.7 wt.%) even after the reaction with bisphosphonate groups of PEG-Ner.

Atomic absorption spectroscopy and elemental analysis were used as further methods to characterize the elemental composition of particles (**Table 3**). Experimentally found Fe, Ce, C, and N content was close to theoretical values. The percentage of analyzed Ce (20.1 wt.%) almost corresponded to Ce content (19 wt.%) based on magnetization measurement and assuming CeO$_2$ to be a shell. The Fe content found in γ-Fe$_2$O$_3$/CeO$_x$ nanoparticles (54.2 wt.%) was slightly higher than theoretical value (50 wt.%), probably due to the moderate removal of cerium oxide during particle purification. Carbon analysis revealed 12.7 wt.% of C, indicating that the γ-Fe$_2$O$_3$/CeO$_x$@PEG$_{2,000}$

particles contained 25.4 wt.% of PEG, which means that 63 wt.% of PEG loaded in the reaction mixture was actually attached to the particle surface. Nitrogen content originating from the neridronate groups anchored to the iron oxide surface amounted to 0.5 wt.% (**Table 3**). The discrepancies between elemental analysis and XPS can be attributed to the latter technique only accounting for the particle surface layer and not the particle bulk.

ROS Scavenging by CeO$_x$ and γ-Fe$_2$O$_3$/CeO$_x$@PEG Nanoparticles
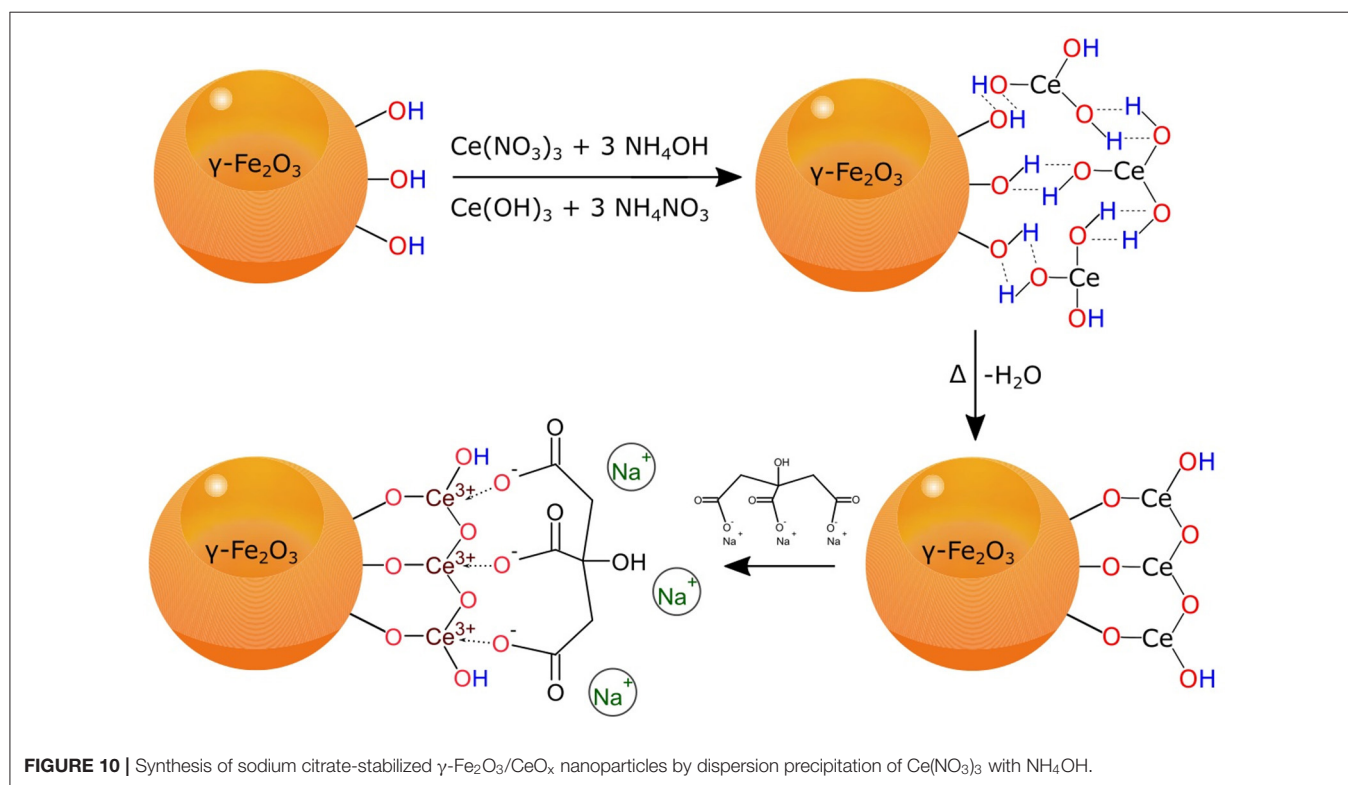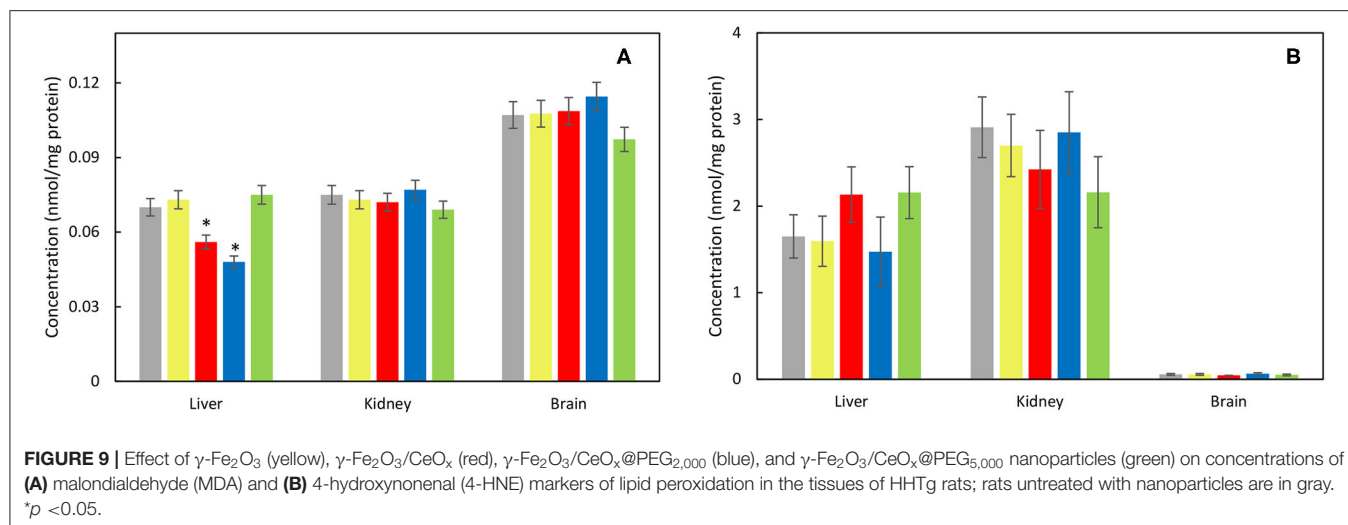
The antioxidant activity (*AA*) of CeO$_x$ particles determined by DPPH assay reached 96%, while that of γ-Fe$_2$O$_3$/CeO$_x$ nanoparticles was 78%, which was a much higher percentage than that of pure γ-Fe$_2$O$_3$ at only 13% (**Table 1**). Both γ-Fe$_2$O$_3$/CeO$_x$@PEG$_{2,000}$ and γ-Fe$_2$O$_3$/CeO$_x$@PEG$_{5,000}$ nanoparticles exhibited similar antioxidant activity, reaching 89 and 85%, respectively. The increase in *AA*, compared to that of γ-Fe$_2$O$_3$/CeO$_x$ particles, can be ascribed to the enhanced surface area of the PEG-modified particles available for scavenging as a result of reduced particle aggregation. A small decrease of antioxidant activity of PEGylated γ-Fe$_2$O$_3$/CeO$_x$ particles compared to that of pure CeO$_x$ can be ascribed to the presence of iron oxide with reduced *AA*.

FIGURE 7 | Effect of γ-Fe$_2$O$_3$ (yellow), γ-Fe$_2$O$_3$/CeO$_x$ (red), γ-Fe$_2$O$_3$/CeO$_x$@PEG$_{2,000}$ (blue), and γ-Fe$_2$O$_3$/CeO$_x$@PEG$_{5,000}$ nanoparticles (green) on activity of **(A)** superoxide dismutase (SOD), **(B)** catalase (CAT), and **(C)** glutathione peroxidase (GPx) in the tissues of HHTg rats; rats untreated with nanoparticles are in gray. *p <0.05 and **p <0.01.

FIGURE 8 | Effect of γ-Fe$_2$O$_3$ (yellow), γ-Fe$_2$O$_3$/CeO$_x$ (red), γ-Fe$_2$O$_3$/CeO$_x$@PEG$_{2,000}$ (blue), and γ-Fe$_2$O$_3$/CeO$_x$@PEG$_{5,000}$ nanoparticles (green) on level of **(A)** reduced (GSH) and **(B)** oxidized forms of glutathione (GSSG) in the tissues of HHTg rats; rats untreated with nanoparticles are in gray. *p <0.05, **p <0.01, and ***p <0.001.

In vivo Effect of γ-Fe$_2$O$_3$/CeO$_x$@PEG Nanoparticles on Oxidative Stress in HHTg Rats

Through biological experiments, effect of γ-Fe$_2$O$_3$, γ-Fe$_2$O$_3$/ CeO$_x$, and γ-Fe$_2$O$_3$/CeO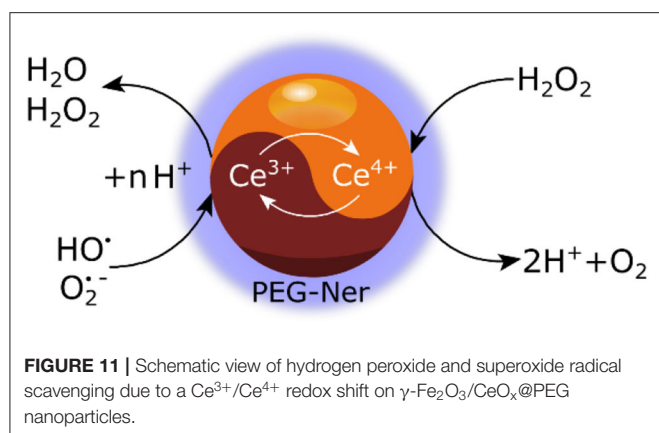$_x$@PEG nanoparticles on oxidative stress and the antioxidant defense in HHTg rats was investigated. Preliminarily, various exposure times were tested (1, 3, and 5 days), with the greatest nanoparticle effect found after 3 days of exposure. Nanoparticle administration did not alter rat body weight, glucose serum levels, triglycerides, total

FIGURE 9 | Effect of γ-Fe_2O_3 (yellow), γ-Fe_2O_3/CeO_x (red), γ-Fe_2O_3/CeO_x@$PEG_{2,000}$ (blue), and γ-Fe_2O_3/CeO_x@$PEG_{5,000}$ nanoparticles (green) on concentrations of **(A)** malondialdehyde (MDA) and **(B)** 4-hydroxynonenal (4-HNE) markers of lipid peroxidation in the tissues of HHTg rats; rats untreated with nanoparticles are in gray. *p <0.05.

FIGURE 10 | Synthesis of sodium citrate-stabilized γ-Fe_2O_3/CeO_x nanoparticles by dispersion precipitation of $Ce(NO_3)_3$ with NH_4OH.

cholesterol, or hepatic enzyme activity (**Table 4**), suggesting that the particles not only avoided damaging the liver but also exhibited good biocompatibility.

Considering oxidative stress status, effect of each nanoparticle type was investigated on liver, kidney cortex, and brain tissues. The activity of antioxidant enzyme SOD increased significantly in the liver after γ-Fe_2O_3/CeO_x@$PEG_{5,000}$ administration as well as in the brain after γ-Fe_2O_3/CeO_x@$PEG_{2,000}$ and in the kidney after γ-Fe_2O_3/CeO_x exposure, compared to the animal control group treated with γ-Fe_2O_3 nanoparticles

(**Figure 7A**). CAT activity increased after the administration of γ-Fe_2O_3/CeO_x@$PEG_{2,000}$ in the brain only (**Figure 7B**). After exposure of γ-Fe_2O_3/CeO_x@$PEG_{2,000}$, the activity of glutathione-dependent enzyme GPx increased in the liver and brain as well as in the liver after γ-Fe_2O_3/CeO_x@$PEG_{5,000}$ nanoparticles administration (**Figure 7C**). In the brain, elevated levels of the reduced form (GSH) of glutathione and decreased levels of the oxidized form (GSSG) after γ-Fe_2O_3/CeO_x@$PEG_{2,000}$ and γ-Fe_2O_3/CeO_x treatment improved oxidative status. The injection of

FIGURE 11 | Schematic view of hydrogen peroxide and superoxide radical scavenging due to a Ce^{3+}/Ce^{4+} redox shift on γ-Fe_2O_3/CeO_x@PEG nanoparticles.

γ-Fe_2O_3/CeO_x@PEG$_{2,000}$ and γ-Fe_2O_3/CeO_x@PEG$_{5,000}$ in HHTg rats also markedly decreased the oxidized form of glutathione in the liver and kidney cortex (**Figures 8A,B**). After γ-Fe_2O_3/CeO_x@PEG$_{2,000}$ particle administration, reduced levels of MDA were observed in the liver (**Figure 9A**). The concentration of another product of lipid peroxidation, 4-HNE, did not change after nanoparticle applications in the case of all tissues examined, indicating no oxidative damage to lipids (**Figure 9B**).

DISCUSSION

In order to obtain magnetic particles possessing antioxidant properties, γ-Fe_2O_3 particles were used as seeds for CeO_x growth (**Figure 10**). Dispersion precipitation of $Ce(NO_3)_3$ with ammonia (pH 11) resulted in the formation of $Ce(OH)_3$ nuclei, which were attached to the γ-Fe_2O_3 surface by hydrogen bonds. This was followed by the conversion of $Ce(OH)_3$ to Ce_2O_3 using a dehydration reaction under heating. The subsequent growth of cerium oxides was stabilized by sodium citrate, resulting in a ceria shell formation around the iron oxide core. XRD confirmed the presence of γ-Fe_2O_3 and CeO_2 crystalline forms in the γ-Fe_2O_3/CeO_x particles. Further coating by PEG$_{2,000}$ did not affect the crystalline structure of the γ-Fe_2O_3/CeO_x nanoparticles or induced crystallization of PEG. Based on a comparison of the high-resolution Ce 3d spectra (**Figure 4**) with data from the literature (Beche et al., 2008), we conclude that cerium in γ-Fe_2O_3/CeO_x nanoparticles coexisted in both Ce^{3+} and Ce^{4+} oxidation states, the latter being the most predominant. The saturation magnetization of starting γ-Fe_2O_3 was relatively comparable to previous reports (Lai et al., 2003; Zasonska et al., 2019), albeit lower than that of bulk maghemite. Because these particles are small in size, they are less magnetic than the same material in bulk, since they contain a higher fraction of metal ions on the particle surface that fail to contribute to net magnetization (Kucheryavy et al., 2013).

In order to stabilize the γ-Fe_2O_3/CeO_x nanoparticles in a culture medium and render them biocompatible, they must be coated with a polymer that is both amphiphilic and hydrophilic. PEG-Ner is an eminently suitable candidate, boasting extremely

high affinity of bisphosphonate groups to metal cations (in our case Ce^{3+}) deposited on the γ-Fe_2O_3 surface. This post-modification of γ-Fe_2O_3/CeO_x nanoparticles differs from one-pot synthesis of dextran-coated nanoceria, which involves the alkaline-based precipitation of cerium oxide from a solution containing cerium salt and dextran (Perez et al., 2008). One of the benefits of CeO_x is its ability to catalytically scavenge ROS, including H_2O_2, hydroxyl, and superoxide radicals due to the high number of surface cerium atoms capable of alternating between Ce^{3+} and Ce^{4+} (**Figure 11**). The further ability of CeO_x to self-regenerate its surface makes the γ-Fe_2O_3/CeO_x@PEG nanoparticles an ideal candidate for *in vivo* ROS scavenging.

In this report, antioxidant activity of γ-Fe_2O_3, γ-Fe_2O_3/CeO_x, and γ-Fe_2O_3/CeO_x@PEG nanoparticles was documented by DPPH assay, a convenient and accurate method for chemically determining radical scavenging ability. γ-Fe_2O_3 itself exhibited relatively low *AA* due to the redox properties of Fe^{3+} ions and the large specific surface area of the particles. In contrast, the ability of cerium oxides attached to the γ-Fe_2O_3 surface to capture radicals was much higher than that of γ-Fe_2O_3. γ-Fe_2O_3/CeO_x@PEG nanoparticles showed significantly higher antioxidant activity (*AA* $\sim$90 %), compared to activity previously reported (*AA* $\sim$45%) for poly(acrylic acid) (PAA)-stabilized Fe_3O_4/CeO_2 core-shell nanoparticles determined by H_2O_2/horse radish peroxidase assay (Wu et al., 2018). Increased *AA* in γ-Fe_2O_3/CeO_x@PEG particles can be induced by differences in the chemical structure and steric orientation of the above polymer coatings, thus restricting the accessibility of DPPH radicals to cerium ions in PAA-coated Fe_3O_4/CeO_2 nanoparticles. This effect may also be partially due to differences in the assays employed.

To determine the antioxidant effect of cerium oxide-decorated magnetic particles, a strain of HHTg rats was deemed the most suitable experimental model given its tendency to exhibit increased oxidative stress in tissues (Malinska et al., 2019). We examined the tissues of the liver, kidney cortex, and brain, where metabolic disorders and changes are associated with metabolic syndrome and diabetes, after administering each nanoparticle type. Based on *in vivo* tests, Fe_2O_3/CeO_x@PEG$_{2,000}$ were found to exhibit a superior antioxidant defense to γ-Fe_2O_3/CeO_x@PEG$_{5,000}$ and γ-Fe_2O_3/CeO_x particles, activating most antioxidant enzymes and reducing the concentration of MDA formed by lipid peroxidation in the liver. Fe_2O_3/CeO_x@PEG$_{2,000}$ exhibited a positive effect on the brain by increasing GSH levels while simultaneously decreasing GSSG concentrations, thus improving oxidative status. Last but not least, Fe_2O_3/CeO_x@PEG particles also demonstrated their capacity to circulate freely within the rat blood stream and thus reach and positively affect target tissues, an especially important asset in preventing the development of diabetic complications.

CONCLUSION

We developed a combination of antioxidant CeO_x nanoparticles and superparamagnetic γ-Fe_2O_3 particles by dual coprecipitation

and oxidation of Fe chlorides and Ce nitrate in alkaline media. The colloidal stability and biocompatibility of the resulting γ-Fe_2O_3/CeO_x particles was clearly boosted by PEGylation. PEG-neridronate proved an excellent stabilizing agent for preventing particle aggregation. γ-Fe_2O_3/CeO_x particles reached the target tissues and ameliorated oxidative stress in tissues. The PEG coating did not affect the autocatalytic properties of nanoceria, given that hydrogen peroxide and peroxyl radicals were able to diffuse through the hydrophilic PEG shell and oxidize Ce^{3+} to Ce^{4+}. Representing another significant advantage, γ-Fe_2O_3/CeO_x@PEG nanoparticles can be prospectively monitored by MRI, facilitating the tracking of cerium oxide delivery to the diseased site and the evaluation of ceria biodistribution. Combining the antioxidant defense properties of cerium oxide with a magnetic carrier thus provides great benefits for magnetic targeting. Compared to the administration of γ-Fe_2O_3/CeO_x@$PEG_{5,000}$, γ-Fe_2O_3/CeO_x, and control γ-Fe_2O_3 nanoparticles, the effect of γ-Fe_2O_3/CeO_x@$PEG_{2,000}$ nanoparticles on parameters of oxidative stress in the brain and liver of HHTg rats was superior. The γ-Fe_2O_3/CeO_x@$PEG_{2,000}$ nanoparticles proved to positively influence oxidative stress in experimental animals, thus providing protection against oxidative damage. As such, the particles offer great potential for reducing complications associated with various diseases accompanied by increased oxidative stress such as cardiovascular disorders, diabetes mellitus, liver steatosis, and inflammatory conditions.

DATA AVAILABILITY STATEMENT

All datasets generated for this study are included in the article/supplementary material.

ETHICS STATEMENT

The animal study was reviewed and approved by the Ethics Committee of the Institute for Clinical and Experimental Medicine, Prague, Czechia.

AUTHOR CONTRIBUTIONS

MM synthesized the particles. IM, HM, DM, MH, and OO performed ROS scavenging and *in vivo* studies of the particles. OP-G, AZ, and EP performed XPS, XRD, and magnetic measurements, respectively. DH supervised the work and together with IM wrote the publication. All authors contributed to the article and approved the submitted version.

FUNDING

REFERENCES

Asati, A., Santra, S., Kaittanis, C., Nath, S., and Perez, J. M. (2009). Oxidase-like activity of polymer-coated cerium oxide nanoparticles. *Angew. Chem. Int. Ed.* 48, 2308–2312. doi: 10.1002/anie.200805279

Beche, E., Charvin, P., Perarnau, D., Abanades, S., and Flamant, G. (2008). Ce 3d XPS investigation of cerium oxides and mixed cerium oxide ($Ce_xTi_yO_z$). *Surf. Interface Anal.* 40, 264–267. doi: 10.1002/sia.2686

Celardo, I., Pedersen, J. Z., Traversa, E., and Ghibelli, L. (2011). Pharmacological potential of cerium oxide nanoparticles. *Nanoscale* 3, 1411–1420. doi: 10.1039/c0nr00875c

Corma, A., Atienzar, P., Garcia, H., and Chane-Ching, J.-Y. (2004). Hierarchically mesostructured doped CeO_2 with potential for solar-cell use. *Nat. Mater.* 3, 394–397. doi: 10.1038/nmat1129

Ivanov, V. K., Shcherbakov, A., and Usatenko, A. (2009). Structure-sensitive properties and biomedical applications of nanodispersed cerium dioxide. *Russ. Chem. Rev.* 78, 855–871. doi: 10.1070/RC2009v078n09ABEH 004058

Jiao, X., Song, H. J., Zhao, H. H., Bai, W., Zhang, L. C., and Lv, Y. (2012). Well-redispersed ceria nanoparticles: promising peroxidase mimetics for H_2O_2 and glucose detection. *Anal. Methods* 4, 3261–3267. doi: 10.1039/c2ay 25511a

Jordan, A., Wust, P., Fähling, H., John, W., Hinz, A., and Felix, R. (1993). Inductive heating of ferrimagnetic particles and magnetic fluids - physical evaluation of their potential for hyperthermia. *Int. J. Hyperthermia* 9, 51–68. doi: 10.3109/02656739309061478

Karakoti, A. S., Kuchibhatla, S. V. N. T., Babu, K. S., and Seal, S. (2007). Direct synthesis of nanoceria in aqueous polyhydroxyl solutions. *J. Phys. Chem.* C 111, 17232–17240. doi: 10.1021/jp076164k

Karakoti, A. S., Singh, S., Kumar, A., Malinska, M., Kuchibhatla, S. V. N. T., Wozniak, K., et al. (2009). PEGylated nanoceria as radical scavenger with tunable redox chemistry. *J. Am. Chem. Soc.* 131, 14144–14145. doi: 10.1021/ja9051087

Korsvik, C., Patil, S., Seal, S., and Self, W. T. (2007). Superoxide dismutase mimetic properties exhibited by vacancy engineered ceria nanoparticles. *Chem. Commun.* 1056–1058. doi: 10.1039/b615134e

Kostiv, U., Lobaz, V., Kučka, J., Švec, P., Sedláček, O., Hrubý, M., et al. (2017). A simple neridronate-based surface coating strategy for upconversion nanoparticles: highly colloidally stable ^{125}I-radiolabeled $NaYF_4$:Yb^{3+}/Er^{3+}@PEG nanoparticles for multimodal *in vivo* tissue imaging. *Nanoscale* 9, 16680–16688. doi: 10.1039/C7NR05456D

Kucheryavy, P., He, J., John, V. T., Maharjan, P., Spinu, L., Goloverda, G. Z., et al. (2013). Superparamagnetic iron oxide nanoparticles with variable size and an iron oxidation state as prospective imaging agents. *Langmuir* 29, 710–716. doi: 10.1021/la3037007

Lai, J., Shafi, K. V. P. M., Loos, K., Ulman, A., Lee, Y., Vogt, T., et al. (2003). Doping γ-Fe_2O_3 nanoparticles with Mn(III) suppresses the transition to the α-Fe_2O_3 structure. *J. Am. Chem. Soc.* 125, 11470–11471. doi: 10.1021/ja035409d

Lee, S. S., Song, W., Cho, M., Puppala, H. L., Nguyen, P., Zhu, H., et al. (2013). Antioxidant properties of cerium oxide nanocrystals as a function of nanocrystal diameter and surface coating. *ACS Nano* 7, 9693–9703. doi: 10.1021/nn4026806

Li, M., Shi, P., Xu, C., Ren, J. S., and Qu, X. G. (2013). Cerium oxide caged metal chelator: anti-aggregation and anti-oxidation integrated H_2O_2-responsive controlled drug release for potential Alzheimer's disease treatment. *Chem. Sci.* 4, 2536–2542. doi: 10.1039/c3sc50697e

Li, Q., Kartikowati, C. W., Horie, S., Ogi, T., Iwaki, T., and Okuyama, K. (2017). Correlation between particle size/domain structure and magnetic properties of highly crystalline Fe_3O_4 nanoparticles. *Sci. Rep.* 7, 9894. doi: 10.1038/s41598-017-09897-5

Malinska, H., Hüttl, M., Oliyarnyk, O., Markova, I., Poruba, M., Racova, Z., et al. (2019). Beneficial effect of troxerutin on metabolic disorders in a non-obese model of metabolic syndrome. *PLoS ONE* 14, e0220377. doi: 10.1371/journal.pone.0220377

Moskvin, M., and Horák, D. (2016). Carbohydrate-modified magnetic nanoparticles for radical scavenging. *Physiological Res.* 65 (Suppl. 2), S243–S252. doi: 10.33549/physiolres.933426

Perez, J. M., Asati, A., Nath, S., and Kaittanis, C. (2008). Synthesis of biocompatible dextran-coated nanoceria with pH-dependent antioxidant properties. *Small* 4, 552–556. doi: 10.1002/smll.200700824

Pirmohamed, T., Dowding, J. M., Singh, S., Wasserman, B., Heckert, E., Karakoti, A. S., et al. (2010). Nanoceria exhibit redox state-dependent catalase mimetic activity. *Chem. Commun.* 46, 2736–2738. doi: 10.1039/b922024k

Pop-Georgievski, O., Zimmermann, R., Kotelnikov, I., Proks, V., Romeis, D., Kučka, J., et al. (2018). Impact of bioactive peptide motifs on molecular structure, charging, and nonfouling properties of poly(ethylene oxide) brushes. *Langmuir* 34, 6010–6020. doi: 10.1021/acs.langmuir.8b00441

Poprac, C., Jomova, K., Simunkova, M., Kollar, V., Rhodes, C. J., and Valko, M. (2017). Targeting free radicals in oxidative stress-related human diseases. *Trends Pharmacol. Sci.* 38, 592–607. doi: 10.1016/j.tips.2017.04.005

Rehman, K., and Akash, M. S. H. (2017). Mechanism of generation of oxidative stress and pathophysiology of type 2 diabetes mellitus: how are they interlinked? *J. Cell Biochem.* 118, 3577–3585. doi: 10.1002/jcb.26097

Schieber, M., and Chandel, N. S. (2014). ROS function in redox signaling and oxidative stress. *Curr. Biol.* 24, R453–R462. doi: 10.1016/j.cub.2014.03.034

Shatan, A. B., Venclíková, K., Zasonska, B. A., Patsula, V., Pop-Georgievski, O., Petrovský, E., et al. (2019). Antibacterial silver-conjugated magnetic nanoparticles: design, synthesis and bactericidal effect. *Pharm. Res.* 36, 147–159. doi: 10.1007/s11095-019-2680-x

Stambouli, A. B., and Traversa, E. (2002). Solid oxide fuel cells (SOFCs): a review of an environmentally clean and efficient source of energy. *Renew. Sust. Energ. Rev.* 6, 433–455. doi: 10.1016/S1364-0321(02)00014-X

Toth, G. B., Varallyay, C. G., Horvath, A., Bashir, M. R., Choyke, P. L., Daldrup-Link, H. E., et al. (2017). Current and potential imaging applications of Ferumoxytol for magnetic resonance imaging HHS public access. *Kidney Int.* 92, 47–66. doi: 10.1016/j.kint.2016.12.037

Turin-Moleavin, I.-A., Fifere, A., Lungoc, A.-L., Rosca, I., Coroaba, A., Peptanariu, D., et al. (2019). *In vitro* and *in vivo* antioxidant activity of

the new magnetic-cerium oxide nanoconjugates. *Nanomaterials* 9, 1565. doi: 10.3390/nano9111565

Walkey, C., Das, S., Seal, S., Erlichman, J., Heckman, K., Ghibelli, L., et al. (2015). Catalytic properties and biomedical applications of cerium oxide nanoparticles. *Environ. Sci. Nano*, 2, 33–53. doi: 10.1039/C4EN00138A

Weaver, J. D., and Stabler, C. L. (2015). Antioxidant cerium oxide nanoparticle hydrogels for cellular encapsulation. *Acta Biomater.* 16, 136–144. doi: 10.1016/j.actbio.2015.01.017

Wu, Y., Yang, Y., Zhao, W., Xu, Z. P., Little, P. J., Whittaker, A. K., et al. (2018). Novel iron oxide–cerium oxide core–shell nanoparticles as a potential theranostic material for ROS related inflammatory diseases. *J. Mater. Chem. B* 6, 4937–4951. doi: 10.1039/C8TB00022K

Xu, C., Lin, Y., Wang, J., Wu, L., Wei, W., Ren, J., et al. (2013). Nanoceria-triggered synergetic drug release based on CeO_2-capped mesoporous silica host-guest interactions and switchable enzymatic activity and cellular effects of CeO_2. *Adv. Healthcare Mater.* 2, 1591–1599. doi: 10.1002/adhm.201200464

Xu, C., and Qu, X. (2014). Cerium oxide nanoparticle: a remarkably versatile rare earth nanomaterial for biological applications. *NPG Asia Mater.* 6, e90. doi: 10.1038/am.2013.88

Zalipsky, S. (1995). Chemistry of polyethylene glycol conjugates with biologically active molecules. *Adv. Drug Deliv. Rev.* 16, 157–182. doi: 10.1016/0169-409X(95)00023-Z

Zasonska, B. A., Líšková, A., Tulinská, J., Pop-Georgievski, O., Ciampor, F., Vávra, I., et al. (2016). Functionalized porous silica&maghemite core-shell nanoparticles for applications in medicine: design, synthesis and immunotoxicity. *Croat. Med. J.* 57, 165–178. doi: 10.3325/cmj.2016.57.165

Zasonska, B. A., Pustovyy, V. I., Babinskiy, A. V., Palyvoda, O. M., Chekhun, V. F., Todor, I., et al. (2019). Combined antitumor effect of surface-modified superparamagnetic maghemite nanoparticles and a vitamin E derivative on experimental Walker-256 mammary gland carcinosarcoma. *J. Magn. Magn. Mater.* 471, 381–387. doi: 10.1016/j.jmmm.2018.10.006

Zhang, F., Wang, P., Koberstein, J., Khalid, S., and Chan, S. W. (2004). Cerium oxidation state in ceria nanoparticles studied with X-ray photoelectron spectroscopy and absorption near edge spectroscopy. *Surf. Sci.* 563, 74–82. doi: 10.1016/j.susc.2004.05.138